In conclusion, we have succeeded in the development of the ruthenium-based metathesis catalyst **4**, which exhibits excellent metathesis activity, without any loss of stability in air. These findings once again demonstrate that seemingly small variations in ligand structure can result in significant improvements in catalysis.

Experimental Section

4: CuCl (21 mg, 0.22 mmol) and then **1** (168 mg, 0.20 mmol) in CH_2Cl_2 (4 mL total) were added to a solution of **8** (94 mg, 0.39 mmol) in CH_2Cl_2 (16 mL) in a glove box. This reaction mixture was stirred for 1 h at 40°C. The reaction mixture was concentrated in vacuo. The residue was dissolved in a minimum volume of CH_2Cl_2, passed through a Pasteur pipette containing a plug of cotton, and concentrated in vacuo. The residue was purified by flash chromatography on silica gel (4:1 hexane/MTBE) to afford **4** (99 mg, 71%). ^1H NMR (CD_2Cl_2): $\delta = 0.81$ (d, $J = 6.2$ Hz, 6H), 2.15–2.72 (br, 18H), 4.16 (s, 4H), 4.36 (septet, $J = 6.2$ Hz, 1H), 6.92 (dd, $J = 0.9$, 7.3 Hz, 1H), 6.99 (t, $J = 7.5$ Hz, 1H), 7.06 (br, 4H), 7.31–7.42 (m, 6H), 16.60 ppm (s, 1H); ^{13}C NMR (CD_2Cl_2): $\delta = 19.6$, 20.5, 51.2, 77.0, 120.9, 123.1, 127.3, 128.1, 128.6, 128.8, 128.9, 131.1, 132.8, 137.8, 138.5, 138.9, 139.3, 147.7, 148.5, 209.8, 297.4 ppm; IR (film): $\tilde{\nu} = 3492$ (br), 1702 (w), 1605 (w), 1481 (m), 1449 (m), 1422 (m), 1263 (s), 1105 (m) cm^{-1}; HRMS *m/z* calcd for $C_{37}H_{42}ON_2Cl_2{}^{102}Ru$: [$M^+$] 702.1711, found: 702.1719; elemental analysis calcd (%) for $C_{37}H_{42}ON_2Cl_2Ru \cdot 1/2\,H_2O$: C 62.44, H 6.09, N 3.94; found: C 62.32; H 5.97, N 3.88.

Received: April 22, 2002 [Z19143]

[1] a) M. Schuster, S. Blechert, *Angew. Chem.* **1997**, *109*, 2124; *Angew. Chem. Int. Ed. Engl.* **1997**, *36*, 2036; b) S. K. Armstrong, *J. Chem. Soc. Perkin Trans. 1* **1998**, 371; c) R. H. Grubbs, S. Chang, *Tetrahedron* **1998**, *54*, 4413; d) A. Fürstner, *Angew. Chem.* **2000**, *112*, 3140; *Angew. Chem. Int. Ed.* **2000**, *39*, 3012; e) T. M. Trnka, R. H. Grubbs, *Acc. Chem. Res.* **2001**, 34, 18–29.

[2] a) W. A. Herrmann, M. Speigler, W. C. Schattenmann, T. Westcamp, *Angew. Chem.* **1998**, *110*, 2631; *Angew. Chem. Int. Ed.* **1998**, *37*, 2490; b) W. A. Hermann, T. Westcamp, L. Ackermann, F. J. Kohl, A. Fürstner, *Tetrahedron Lett.* **1999**, *40*, 4787; c) J. Huang, E. D. Stevens, S. P. Nolan, J. L. Pedersen, *J. Am. Chem. Soc.* **1999**, *121*, 2674; d) M. Scholl, S. Ding, C. W. Lee, R. H. Grubbs, *Org. Lett.* **1999**, *1*, 953; e) M. S. Sanford, M. Ulman, R. H. Grubbs, *J. Am. Chem. Soc.* **2001**, *123*, 749; f) M. S. Sanford, J. A. Love, R. H. Grubbs, *J. Am. Chem. Soc.* **2001**, *123*, 6543.

[3] a) S. B. Garber, J. S. Kingsbury, B. L. Gray, A. H. Hoveyda, *J. Am. Chem. Soc.* **2000**, *122*, 8168; b) S. Gessler, S. Randl, S. Blechert, *Tetrahedron Lett.* **2000**, *41*, 9973.

[4] a) S. Randl, S. Gessler, H. Wakamatsu, S. Blechert, *Synlett* **2001**, 430; b) S. Imhof, S. Randl, S. Blechert, *Chem. Commun.* **2001**, 1692; c) S. Randl, N. Buschmann, S. J. Connon, S. Blechert, *Synlett* **2001**, 1547; d) S. Randl, S. J. Connon, S. Blechert, *Chem. Commun.* **2001**, 1796; e) S. J. Connon, S. Blechert, *Bioorg. Med. Chem. Lett.* **2002**, in press.

[5] H. Wakamatsu, S. Blechert, *Angew. Chem.* **2002**, 114, 832; *Angew. Chem. Int. Ed.* **2002**, 41, 794.

[6] M. M. G. Antonisse, B. H. M. Snellink-Ruël, A. C. Ion, J. F. J. Engbersen, D. N. Reinhoudt, *J. Chem. Soc. Perkin Trans. 2*, **1999**, 1211.

[7] C. W. Bielawski, R. H. Grubbs, *Angew. Chem.* **2000**, 112, 3025; *Angew. Chem. Int. Ed.* **2000**, 39, 2903.

Photochemical Sensing of NO_2 with SnO_2 Nanoribbon Nanosensors at Room Temperature**

Matt Law, Hannes Kind, Benjamin Messer,
Franklin Kim, and Peidong Yang*

A major area of application for nanowires and nanotubes is likely to be the sensing of important molecules, either for medical or environmental health purposes. The ultrahigh surface-to-volume ratios of these structures make their electrical properties extremely sensitive to surface-adsorbed species, as recent work has shown with carbon nanotubes,[1, 2] functionalized silicon nanowires and metal nanowires.[3, 4] Chemical nanosensors are interesting because of their potential for detecting very low concentrations of biomolecules or pollutants on platforms small enough to be used in vivo or on a microchip. Here we report the development of photochemical NO_2 sensors that work at room temperature and are based on individual single-crystalline SnO_2 nanoribbons.

Tin dioxide is a wide-bandgap (3.6 eV) semiconductor. For n-type SnO_2 single crystals, the intrinsic carrier concentration is primarily determined by deviations from stoichiometry in the form of equilibrium oxygen vacancies, which are predominantly atomic defects.[5] The electrical conductivity of nanocrystalline SnO_2 depends strongly on surface states produced by molecular adsorption that results in space-charge layer changes and band modulation.[6] NO_2, a combustion product that plays a key role in tropospheric ozone and smog formation, acts as an electron-trapping adsorbate on SnO_2 crystal faces and can be sensed by monitoring the electrical conductance of the material. Because NO_2 chemisorbs strongly on many metal oxides,[7] commercial sensors based on particulate or thin-film SnO_2 operate at 300–500°C to enhance the surface molecular desorption kinetics and continuously "clean" the sensors.[8] The high-temperature operation of these oxide sensors is not favorable in many cases, particularly in an explosive environment. We have found that the strong photoconducting response of individual single-crystalline SnO_2 nanoribbons makes it possible to achieve equally favorable adsorption–desorption behavior at room temperature by illuminating the devices with ultraviolet (UV) light of energy near the SnO_2 bandgap. The active desorption process is thus photoinduced molecular desorption (Figure 1).[9]

---

[*] Prof. P. Yang, M. Law, Dr. H. Kind, B. Messer, F. Kim
Department of Chemistry
University of California, Berkeley
Berkeley, CA 94720-1460 (USA)
Fax: (+1) 510-642-7301
E-mail: p_yang@uclink.berkeley.edu

[**] This work was supported by the Camille and Henry Dreyfus Foundation, 3M Corporation, the National Science Foundation, and the University of California, Berkeley. P.Y. is an Alfred P. Sloan Research Fellow. Work at the Lawrence Berkeley National Laboratory was supported by the Office of Science, Basic Energy Sciences, Division of Materials Science of the US Department of Energy. We thank the National Center for Electron Microscopy for the use of their facilities.

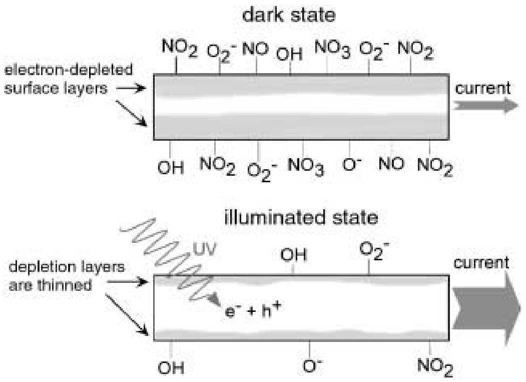

Figure 1. A schematic longitudinal cross-section of a nanoribbon in the dark and in UV light. In the illuminated state, photogenerated holes recombine with trapped electrons at the surface, desorbing NO_2 and other electron-trapping species: $h^+ + NO^{2-}_{2(ads)} \rightarrow NO_{2(gas)}$. The space charge layer thins, and the nanoribbon conductivity rises. Ambient NO_2 levels are tracked by monitoring changes in conductance in the illuminated state.

SnO_2 nanoribbons were synthesized using a simple thermal deposition process.[10–12] The nanoribbons are single crystalline with a rutile structure. Field emission scanning electron microscopy (FE-SEM) and transmission electron microscopy (TEM) imaging (Figure 2) reveal they are tens of μm long with rectangular cross sections, typically 80–120 nm wide and 10–30 nm thick. High-resolution (HRTEM) analysis confirms that they grow approximately along the [101] direction and present the $(10\bar{1})$ and (010) rutile planes as surface facets along the growth axis and the (201) plane on the ends. The as-synthesized nanoribbons were deposited from ethanol solution onto prefabricated gold electrodes in a four-terminal configuration, and SEM imaging was used to ensure that only a single nanowire bridged the electrodes of each sample (Figure 2C). The samples were electrically connected to a Keithley source-measure unit and mounted in a home-made test chamber for gas sensing measurements.

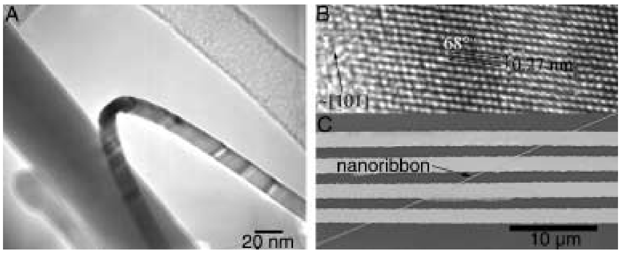

Figure 2. A) Low-resolution TEM image of a thin SnO_2 nanoribbon. The short side of the rectangle is visible near the twist. B) HRTEM image looking down onto the (010) side surface plane near the edge of a nanoribbon, with the lattice spacing and growth direction indicated in agreement with ref. [10]. The angle between the (101) and (011) plane is 68°. C) Typical FE-SEM image of a NO_2-sensing nanoribbon device on an insulating substrate.

We analyzed the optoelectronic response of these devices in air and NO_2 environments in order to probe their chemical-sensing abilities. The behavior of a representative nanoribbon is shown in Figure 3A. In the dark and in pure air (troughs of blue curve), the nanoribbons had resistances ranging from 500 MΩ to 12 GΩ.[13] When exposed to UV light with a wavelength of 254 nm (intensity = 0.63 mW cm^{-2}; large peak of blue curve), which corresponds to an energy significantly greater than the SnO_2 bandgap (345 nm), the nanosensor conductance increased by three to four orders of magnitude and stabilized within 1–2 min. The conductance rise is due both to the generation of photocurrent, which directly increases the number of free carriers within the device, and to photodesorption of surface species (mostly O_2- and H_2O-derived),[14] with a concomitant thinning of the electron depletion layer near the nanoribbon surface. This phenomenon was also observed recently in ZnO nanowires.[15]

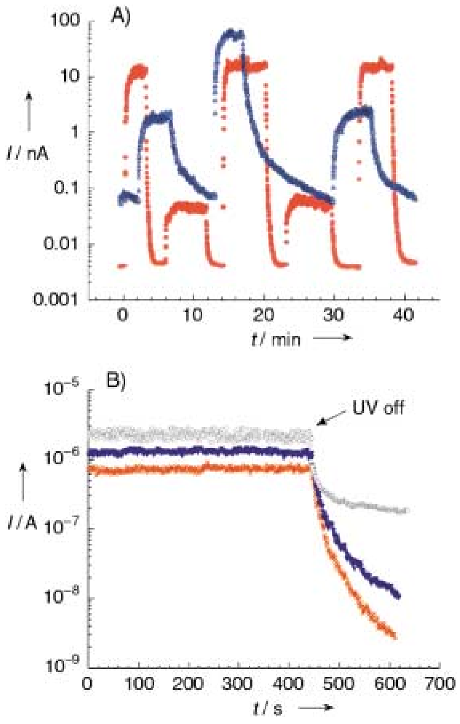

Figure 3. A) Photoresponse of a single nanoribbon in pure air (blue) and 100 ppm NO_2 (red). The large peaks of both curves correspond to 254 nm UV illumination, the small peaks to 365 nm illumination, and the troughs to dark current. The blue-to-red signal ratio is 45:1 under 365 nm light and 4:1 under 254 nm light. Note the shorter decay times in the presence of NO_2. Bias is 1.0 V. B) Initial decay of the 254 nm photoresponse for a nanoribbon in 8×10^{-5} mbar vacuum (gray), air (blue), and 100 ppm (red) NO_2. 99.9% decay in vacuum took over 4 h, while the signals in air and NO_2 decayed fully in about 300 and 200 s, respectively. Bias is 0.5 V.

The effect was fully reversible when the light was turned off, with 99.9% decay of the photoresponse in 300–500 s. Illumination with 365 nm radiation (intensity = 0.5 mW cm^{-2}; small peaks of blue curve in Figure 3A) also resulted in a photoresponse, typically a 10- to 100-fold increase in the nanoribbon conductance, with slightly faster rise and decay constants than in the 254 nm case. The effect of the 365 nm radiation, which corresponds to an energy slightly smaller than the bandgap, is likely due to the presence of surface states that populate the energy gap. The photoswitching behavior was reproducible at both UV wavelengths indefinitely.

When the nanoribbons were tested in an atmosphere of 100 ppm NO_2 in air (Matheson Tri-Gas), resistance values were higher for all three states—dark, 254-exposed and 365-

exposed (red curve in Figure 3 A)—compared to their respective values in pure air. The photoresponse decays were also significantly faster in 100 ppm NO_2, with 99.9 % falloffs in 35 – 50 s. This faster decay rate can be attributed to the strong adsorption and electron-trapping interaction of NO_2 on SnO_2 surfaces. Figure 3 B shows the photocurrent decay for a single nanosensor in vacuum, air, and 100 ppm NO_2 environments after exposure to a 254 nm light source. Decay times get shorter and dark currents smaller in the sequence vacuum →air →100 ppm NO_2, which reflects the availability of gas-phase molecules for adsorption and the better oxidizing ability of NO_2 relative to O_2. Comparing the two curves in Figure 3 A shows that the current/conductance difference between the device operating in air and in 100 ppm NO_2 was larger under 365 nm than under 254 nm illumination, so that greater sensitivity to NO_2 occurred using the longer wavelength. The precise reason for this tendency is unknown, but it was observed for all samples and the best nanosensors were operated under continuous 365 nm light during sensing experiments. Note that UV is vital for sensing, as NO_2 adsorption is irreversible in the dark. Figure 4 plots the response ratios of nine of the nanosensors to concentrations of NO_2 from 2 – 100 ppm.

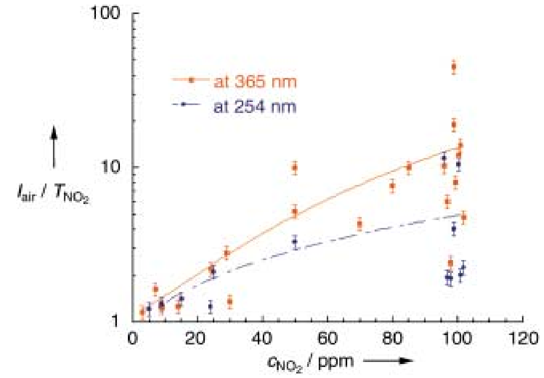

Figure 4. Responses for nine samples at different NO_2 concentrations. Only those samples with response ratios (I_{air}/I_{NO_2}) greater than 8 at 100 ppm NO_2 were tested at lower concentrations. The fits to the data are suggestive only, as the individual nanoribbons showed nonlinear sensing behavior.

The nature of the electrical contacts between the SnO_2 nanoribbons and the gold electrodes is important to understanding the behavior of these devices, since the contacts dictate whether the metal – semiconductor junctions or the semiconducting nanoribbons themselves are responsible for the photochemical response. Rectifying current (I) versus voltage (V) behavior was observed for many of the nanosensors, indicating that the contacts act as metal – semiconductor Schottky diodes. This suggests that the overall current response in many of the nanowire sensors resulted from four combined effects: 1) photoconductivity of the nanoribbon, 2) NO_2 adsorption on the nanoribbon, 3) photoresponse of the junctions, and 4) modulation of the Schottky potential barriers due to NO_2 activity in the junction regions. Thus, for the samples with non-ohmic contacts, sensing was a collective effect of the nanoribbon and the junctions.

Although most of the nanoribbon sensing devices showed rectifying behavior, samples with ohmic contacts have also been tested with nearly linear I-V characteristics under 254 nm irradiation (Figure 5 A). Experiments with these samples (Figure 5 B) gave clear evidence that the nanoribbon is the active sensing element when the contacts are ohmic. This suggests that the nanoribbons may dominate the photochemical response even in the non-ohmic devices.

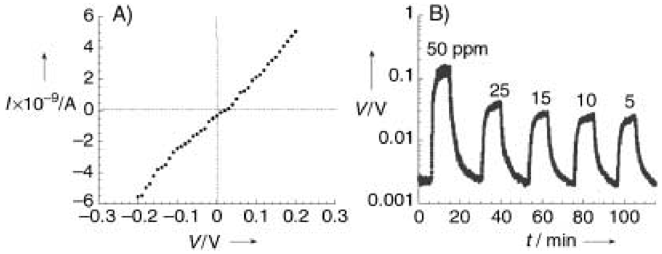

Figure 5. A) A nanoribbon device showing nearly ohmic behavior under 254 nm UV light in 100 ppm NO_2. In this case, the device properties depend predominantly on the nanoribbon itself. B) Cycling the nanoribbon between decreasing concentrations of NO_2 (peaks) and 8×10^{-5} mbar vacuum (troughs) under 254 nm UV light. The resolution limit of the sensor is 5 – 10 ppm. Current was held constant at 5 nA.

To determine the behavior of the nanosensors under realistic operating conditions, they were cycled through different NO_2 concentrations under continuous 365 nm illumination and in gas flows of 150 sccm (standard cubic centimeters per minute). The devices showed greater sensitivity to low NO_2 concentrations ($<$ 15 ppm), while higher concentrations caused smaller signal changes as the nanoribbon surface became saturated with NO_2. In addition, the signal noise decreased at higher concentrations.

The resolution limit achieved by these nanoribbons fell between 2 and 10 ppm for the six samples that showed response ratios of 8 or better at 100 ppm NO_2 under 365 nm light. Figure 6 shows the conductance response of one nanosensor cycled between pure air and 3 ppm NO_2. Even with the low signal-to-noise ratio, current steps can be clearly distinguished as the NO_2 was turned on and off. This behavior was stable for more than 20 cycles without appreciable drift and

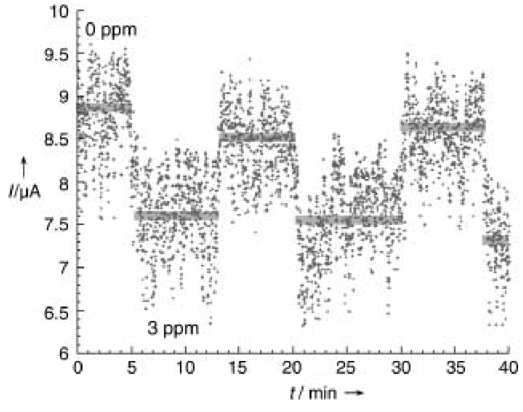

Figure 6. Cycling a nanosensor near its resolution limit under 365 nm light. NO_2 concentrations are indicated. Horizontal bars are signal averages. The average signal difference for the three cycles is 16 %. Bias is 0.5 V.

with response times of less than one minute. The average response ratio at 3 ppm NO_2 was 1.16.

Individual SnO_2 nanoribbons are small, fast and sensitive devices for detecting ppm-level NO_2 at room temperature under UV light. These nanodevices can be operated under laboratory conditions over many cycles without loss of sensitivity. The advantages of low-temperature, potentially drift-free operation make SnO_2 nanoribbons good candidates for miniaturized, ultrasensitive gas sensors in many applications. Further sensitivity increases should be achievable by using thinner nanoribbons, developing ohmic SnO_2–metal contacts and decorating these structures with catalysts. With such innovations, the chemical detection of single molecules on nanowires may soon be within reach.

Received: February 22, 2002 [Z18752]

[1] a) J. Kong, N. Franklin, C. Wu, S. Pan, K. J. Cho, H. Dai, *Science* **2000**, *287*, 622; b) R. J. Chen, N. R. Franklin, J. Kong, J. Cao, T. W. Tombler, Y. Zhang, H. Dai, *Appl. Phys. Lett.* **2001**, *79*, 2258.

[2] P. G. Collins, K. Bradley, M. Ishigami, A. Zettl, *Science* **2000**, *287*, 1801.

[3] Y. Cui, Q. Wei, H. Park, C. M. Lieber, *Science* **2001**, *293*, 1289.

[4] F. Favier, E. C. Walter, M. P. Zach, T. Benter, R. M. Penner, *Science* **2001**, *293*, 2227.

[5] C. G. Founstadt, R. H. Rediker, *J. Appl. Phys.* **1971**, *42*, 2911.

[6] O. V. Safonova, M. N. Rumyantseva, L. I. Ryabova, M. Labeau, G. Delabouglise, A. M. Gaskov, *Mater. Sci. Eng. B* **2001**, *85*, 43.

[7] See for example: a) V. E. Henrich, P. A. Cox, *The Surface Science of Metal Oxides*, Cambridge University Press, Cambridge, **1994**; b) J. Tamaki, M. Nagaishi, Y. Teraoka, N. Miura, N. Yamazoe, L. Moriya, Y. Nakamura, *Surf. Sci.* **1989**, *221*, 183.

[8] N. Barsan, M. S. Berberich, W. Goepel, *Fresenius J. Anal. Chem.* **1999**, *365*, 287.

[9] E. Comini, A. Cristalli, G. Faglia, G. Sberveglieri, *Sens. Actuators B* **2000**, *65*, 260.

[10] Z. R. Dai, Z. W. Pan, Z. L. Wang, *Solid State Commun.* **2001**, *118*, 351.

[11] M. Huang, Y. Wu, H. Feick, N. Tran, E. Weber, P. Yang, *Adv. Mater.* **2001**, *13*, 113.

[12] M. Huang, S. Mao, H. Feick, H. Yan, Y. Wu, H. Kind, E. Weber, R. Russo, P. Yang, *Science* **2001**, *292*, 1897.

[13] Resistivity estimates were made difficult by uncertainties in the cross-sectional area of a nanoribbon dispersed across the electrodes of a device. Dark values in air fell from 1 to 500 Ωcm. The resistivity values of the nanoribbons are highly dependent on ambient light levels, the chemical state of the surface and the quality of the electrical contacts; they cannot be directly compared with bulk values. We therefore use only conductance values here.

[14] N. Yamazoe, J. Fuchigami, M. Kishikawa, T. Seiyama, *Surf. Sci.* **1978**, *86*, 335.

[15] H. Kind, H. Yan, B. Messer, M. Law, P. Yang, *Adv. Mater.* **2002**, *14*, 158.

Chirality and Macroscopic Polar Order in a Ferroelectric Smectic Liquid-Crystalline Phase Formed by Achiral Polyphilic Bent-Core Molecules**

Gert Dantlgraber, Alexei Eremin, Siegmar Diele, Anton Hauser, Horst Kresse, Gerhard Pelzl, and Carsten Tschierske*

Materials with a macroscopic polar order have a variety of useful properties, such as piezo- and pyroelectricity and second-order nonlinear optical activity[1, 2] Especially ferroelectric (FE) and antiferroelectric (AF) liquid crystalline (LC) materials are of great interest, because they can be rapidly switched between different states by means of external electrical fields.[3, 4] These properties makes them useful for numerous applications, such as electrooptic devices, information storage, switchable NLO (nonlinear optic) devices and light modulators, which may be of interest for optical computing and other future technologies. At first, smectic LC phases with tilted arrangements of nonracemic chiral rodlike and disclike molecules have been used for this purpose and for a long time molecular chirality appeared to be essential for obtaining such materials.[3] However, the discovery by Niori et al. that bent-core mesogenic compounds (banana-shaped molecules) without molecular chirality, can also organize in fluid smectic phases with a polar order opened a new area in the field of LC research.[5, 6] The polar structure of the smectic layers of such molecules is provided by the dense directed packing of their bent aromatic cores. However, to escape from a macroscopic polar order the bent direction in adjacent layers is antiparallel, so that the layer polarization alternates from layer to layer, which leads to a macroscopic apolar AF structure.[7] In most cases of such mesophases the molecules are additionally tilted relative to the layer normal.[8] Therefore these phases (also known as "B2"-phases) can be described as tilted smectic phases (SmC) with a polar order of the molecules (P) within the layers, and an antiparallel polarization in adjacent layers (A), which leads to the notation $SmCP_A$. Because the molecules in adjacent layers can have either a synclinic (molecules in adjacent layers are tilted in the same direction, C_S) or an anticlinic (molecules in adjacent layers are tilted in opposite directions, C_A) interlayer correlation, the four different phase structures shown in Figure 1 may result for such mesophases.[7] Usually, the AF phases represent the ground states, whereas the FE states (SmC_SP_F and SmC_AP_F) can only be achieved after

---

[*] Prof. Dr. C. Tschierske, G. Dantlgraber
Institute of Organic Chemistry
Martin-Luther-University Halle-Wittenberg
Kurt-Mothes-Strasse 2, 06120 Halle (Germany)
Fax: (+49) 345-55-27223
E-mail: tschierske@chemie.uni-halle.de

A. Eremin, Dr. S. Diele, Dr. A. Hauser, Prof. Dr. H. Kresse, Prof. Dr. G. Pelzl
Institute of Physical Chemistry
Martin-Luther-University Halle-Wittenberg

[**] This work was supported by the Deutsche Forschungsgemeinschaft and the Fonds der Chemischen Industrie.